Monthly Notices
of the
ROYAL ASTRONOMICAL SOCIETY

MNRAS **480,** 1096–1105 (2018)
Advance Access publication 2018 July 23

doi:10.1093/mnras/sty1955

The clustering of the SDSS-IV extended Baryon Oscillation Spectroscopic Survey DR14 quasar sample: measuring the anisotropic baryon acoustic oscillations with redshift weights

Fangzhou Zhu,[1⋆] Nikhil Padmanabhan,[1] Ashley J. Ross,[2] Martin White,[3] Will J. Percival,[4] Rossana Ruggeri,[4] Gong-bo Zhao,[4,5] Dandan Wang,[5] Eva-Maria Mueller,[4] Etienne Burtin,[7] Héctor Gil-Marín,[8,9] Julian Bautista,[10] Florian Beutler,[4,6] Jonathan Brinkmann,[11] Joel R. Brownstein,[10] Kyle Dawson,[10] Axel de la Macorra,[12] Graziano Rossi,[13] Donald P. Schneider,[14,15] Rita Tojeiro,[16] and Yuting Wang[4,5]

Affiliations are listed at the end of the paper

Accepted 2018 July 19. Received 2018 July 10; in original form 2018 May 3

ABSTRACT

We present an anisotropic analysis of baryon acoustic oscillation (BAO) signal from the Sloan Digital Sky Survey IV extended Baryon Oscillation Spectroscopic Survey Data Release 14 quasar sample. The sample consists of 147 000 quasars distributed over a redshift range of $0.8 < z < 2.2$. We apply the redshift weights technique to the clustering of quasars in this sample and achieve a 4.6 per cent measurement of the angular distance measurement D_M at $z = 2.2$ and Hubble parameter H at $z = 0.8$. We parametrize the distance–redshift relation, relative to a fiducial model, as a Taylor series. The coefficients of this expansion are used to reconstruct the distance–redshift relation and obtain distance and Hubble parameter measurements at all redshifts within the redshift range of the sample. Reporting the result at two characteristic redshifts, we determine $D_M(z = 1) = 3405 \pm 305\,(r_{\rm d}/r_{\rm d,\,fid})$ Mpc, $H(z = 1) = 120.7 \pm 7.3\,(r_{\rm d,fid}/r_{\rm d})$ km s^{-1} Mpc^{-1} and $D_M(z = 2) = 5325 \pm 249\,(r_{\rm d}/r_{\rm d,\,fid})$ Mpc, $H(z = 2) = 189.9 \pm 32.9\,(r_{\rm d,fid}/r_{\rm d})$ km s^{-1} Mpc^{-1}. These measurements are highly correlated. We assess the outlook of BAO analysis from the final quasar sample by testing the method on a set of mocks that mimic the noise level in the final sample. We demonstrate on these mocks that redshift weighting shrinks the measurement error by over 25 per cent on average. We conclude redshift weighting can bring us closer to the cosmological goal of the final quasar sample.

Key words: dark energy – distance scale – cosmology: observations.

1 INTRODUCTION

Baryon acoustic oscillations (BAO) in the distribution of the galaxies are a powerful tool to map the expansion history of the universe via a 'standard ruler' in galaxy clustering (Peebles & Yu 1970; Sunyaev & Zeldovich 1970; Bond & Efstathiou 1987; Hu & Sugiyama 1996; Eisenstein & Hu 1998). Pressure waves prior to recombination imprint a characteristic scale in the matter clustering at the radius of the sound horizon r_d when the photons and baryons decouple shortly after recombination. The BAO manifests itself today in the two-point matter correlation function as an 'acoustic peak' of roughly 150 Mpc. This feature of known length can be used as a standard ruler to constrain the distance–redshift relation and the expansion history of the universe.

Different tracers of the underlying dark matter distribution have been used successfully to measure the peak. These analyses include galaxies (Alam et al. 2017), the Ly α forest (Delubac et al. 2015; Bautista et al. 2017), voids (Kitaura et al. 2016), and quasar-Ly α forest cross correlations (Font-Ribera et al. 2014). Since the first detection of BAO (Cole et al. 2005; Eisenstein et al. 2005) in the galaxy distribution over a decade ago, galaxy surveys (Blake et al. 2007; Kazin et al. 2010; Percival et al. 2010; Beutler et al. 2011; Padmanabhan et al. 2012; Alam et al. 2017) have been driving the measurement to ever increasing precision. Notably, Baryon Oscillation Spectroscopic Survey (BOSS; Dawson et al. 2013; Alam et al. 2015) as a part of the Sloan Digital Sky Survey III (SDSS-III; Eisen-

⋆ E-mail: fangzhou.zhu@yale.edu

stein et al. 2011) has enjoyed great success in making cosmological distance measurements at the per cent level.

The extended Baryon Oscillation Spectroscopic Survey (eBOSS; Dawson et al. 2016) is a new redshift survey within SDSS-IV (Blanton et al. 2017), the observations for which started in 2014 July. The photometry was obtained on the 2.5-m Sloan Telescope (Gunn et al. 2006) at the Apache Point Observatory in New Mexico, USA. As part of this programme, eBOSS observes quasars that are selected to enable clustering studies. The quasar sample covers a redshift range of $0.8 < z < 2.2$. The final sample is forecasted to produce a 1.6 per cent spherically averaged distance measurement (Zhao et al. 2016). This paper uses the Data Release 14 (DR14) quasar sample whose targeting and observation details are described in Abolfathi et al. (2017).

Samples from current and future generations of BAO surveys such as the eBOSS span a wide redshift range. To improve the resolution of distance–redshift relation measurement, traditional BAO analyses usually split the samples into multiple redshift bins and analyse the signals in these slices. One drawback of splitting the sample into multiple redshift bins is that the signal-to-noise ratio in each bin becomes lower, making the analysis more sensitive to the tails of the likelihood distribution. Furthermore, signals from galaxy pairs across disjoint bin boundaries are lost in such an analysis. While some of these disadvantages may be overcome by properly accounting for all the covariances among the slices, they add to the complexity of the analysis. There is also no consensus on how to optimally split the sample.

To solve the problems faced with binning outlined above, Zhu, Padmanabhan & White (2015) introduced a set of redshift weights to compress the BAO information in the redshift direction on to a small number of 'weighted correlation functions'. Applying the redshift weights to the galaxy pair counts efficiently preserves nearly all the BAO information in the sample, leading to improved constraints of the distance–redshift relation parametrized in a simple generic form over the entire redshift extent of the survey. Zhu et al. (2016) validated the redshift weighting method on BOSS DR12 galaxy mock catalogues. Applying redshift weighting provides tighter distance and Hubble estimates over a sample's redshift range compared with the unweighted single-bin analysis. The method has also been demonstrated to produce robust and unbiased BAO measurements.

This paper applies redshift weighting to the BAO analysis of the eBOSS DR14 quasar sample. These measurements complement the analysis in Ata et al. (2017) and provide a first measurement of $H(z)$ from this sample. The paper has the following structure: Section 2 describes the redshift weights and BAO modelling for the correlation functions. Section 3 describes the data sets and simulations used in this paper. In Section 4, we present the implemented redshift weighting algorithm and describe the fitting model. We present our DR14 data and mock results in Section 5 and show the improvement due to redshift weighting. We share an outlook of the BAO constraints from the final quasar sample in Section 6. We emphasize the efficacy of redshift weighting for such a sample. We summarize our results with a discussion in Section 7.

2 THEORY

2.1 Distance–redshift relation

Following Zhu et al. (2015), we parametrize the distance–redshift relation, relative to a fiducial cosmology, as a Taylor series. Denoting the comoving distance by $\chi(z)$, we have

$$\frac{\chi(z)}{\chi_f(z)} = \alpha_0 \left(1 + \alpha_1 x + \frac{1}{2}\alpha_2 x^2 + \cdots\right). \quad (1)$$

In the above parametrization, $\chi_f(z)$ labels the fiducial comoving radial distance and $x(z) \equiv \chi_f(z)/\chi_f(z_0) - 1$. Here, z_0 is a pivot redshift chosen at convenience within the redshift range of the survey.

Calculating the Hubble parameter as the inverse derivative of the comoving distance, we obtain a relation for $H(z)$ as

$$\frac{H_f(z)}{H(z)} = \alpha_0 \left[1 + \alpha_1 + (2\alpha_1 + \alpha_2)x + \frac{3}{2}\alpha_2 x^2 + \cdots\right]. \quad (2)$$

Once the parameters α_0, α_1, and higher order coefficients are inferred from the sample, it is straightforward to recover the measured distance–redshift relation and Hubble parameter from our expansion. When the fiducial cosmology coincides with the true cosmology, one will measure $\alpha_0 = 1$ with α_1 and all other higher order terms equal to zero.

Truncating the expansion to the first order is sufficient for recovering the distance–redshift relation to sub-percent levels over the redshift range of interest for an assortment of cosmologies. Even for the rather extreme $\Omega_M = 0.2$ and $\Omega_M = 0.4$ cases, the errors are less than 0.3 per cent over the redshift range of the eBOSS DR14 quasar sample $0.8 < z < 2.2$. We will thus focus on α_0 and α_1 and drop all higher order terms in the BAO analysis presented in this paper.

A simple relation exists between our parametrization and the (α, ϵ) or ($\alpha_\perp$, $\alpha_\parallel$) parametrization (Padmanabhan & White 2008; Xu et al. 2013) used in recent BAO analyses (Anderson et al. 2014; Alam et al. 2017). In these analyses, the deformation of the separation vectors between galaxy pairs are parametrized by an 'isotropic dilation' parameter $\alpha(z)$ and an 'anisotropic warping' parameter $\epsilon(z)$. In the plane parallel limit, α and ϵ are related to the comoving distance and Hubble parameter by

$$\alpha(z) = \left[\frac{H_f(z)\chi^2(z)}{H(z)\chi_f^2(z)}\right]^{1/3} \quad (3)$$

$$\epsilon(z) = \left[\frac{H_f(z)\chi_f(z)}{H(z)\chi(z)}\right]^{1/3} - 1. \quad (4)$$

Together with equations (1) and (2), we can write $\alpha(z)$ and $\epsilon(z)$ in terms of α_0 and α_1. Working to linear order in α_1, we have

$$\alpha(z) = \alpha_0 \left(1 + \frac{1}{3}\alpha_1 + \frac{4}{3}\alpha_1 x\right) \quad (5)$$

$$\epsilon(z) = \frac{1}{3}\alpha_1 + \frac{1}{3}\alpha_1 x. \quad (6)$$

2.2 Redshift-weighted correlation function

Modelled on Tegmark, Taylor & Heavens (1997) as an extension of Feldman, Kaiser & Peacock (1994), Zhu et al. (2015) developed the general formalism for a set of redshift weights for BAO analyses. The weights optimize the measurement of the parameters α_0 and α_1 in our distance–redshift relation parametrization. These weights can be expressed as the product of two components as $\mathrm{d}W w_{\ell,i}$. The first component is the commonly used FKP weights in galaxy surveys

$$dW(z) = \left(\frac{\bar{n}}{\bar{n}P + 1}\right)^2 dV(z), \quad (7)$$

where $P = 6000\,h^3\,\mathrm{Mpc}^{-3}$ is the power spectrum evaluated at $k \sim 0.14\,\mathrm{Mpc}^{-1}$. This expression corresponds to the inverse variance of the power spectrum in redshift slices.

The second component $w_{\ell,i}$ is a linear combination of 1 and x. The specific linear combination depends on the parameter (α_0 or α_1, indicated by the subscript i) and the multipoles (monopoles or quadrupoles, indicated by ℓ) in question. The redshift weights are generalizations of the FKP weights produced by up-weighting the regions where the signal is most sensitive to the model parameters, in addition to balancing the quasars by number densities.

The fact that the weights $w_{\ell,i}$ are linear combinations of 1 and x makes it convenient to compute and analyse correlation functions weighted by 1 and x. We construct the '1-weighted' and 'x-weighted' correlation functions as

$$\xi_{\ell,1}(r) = \frac{1}{N}\int \mathrm{d}\mathcal{W}(z)\xi_{\ell,g}(r,z) \tag{8}$$

$$\xi_{\ell,x}(r) = \frac{1}{N}\int \mathrm{d}\mathcal{W}(z)x(z)\xi_{\ell,g}(r,z) \tag{9}$$

where $N = \int \mathrm{d}\mathcal{W}$. The galaxy correlation function $\xi_{\ell,g} = b^2\xi_{\ell,m}$, where b is the galaxy bias.

In these models, the integrals are over the redshift range of the sample. They can be efficiently computed as summations over contributions from discrete redshift slices. We follow the same procedure as in Zhu et al. (2016) and compute the contributions from redshift slices of width $\Delta z = 0.1$ within the redshift range [0.8, 2.2]. In each redshift slice, given α_0 and α_1, we compute $\alpha(z)$ and $\epsilon(z)$ according to equations (5) and 6 at different redshifts. This feature is different from traditional analyses in which α and ϵ values only at the 'effective' redshift of the sample are measured. We will describe how α and ϵ shift and distort the correlation function in Section 2.3.2. Our model parameters α_0 and α_1, which we will obtain directly from our fits to the measured ξ, provide constraints on $\alpha(z)$ and $\epsilon(z)$ given our perturbative model.

2.3 Fitting the correlation function

We fit the correlation function with the ESW template given in Eisenstein, Seo & White (2007a).[1] We will outline the ESW template below and explain its ingredients and how mis-estimate of the cosmology distorts the correlation function and how to model it. The fitting model is similar as in recent BOSS BAO analyses (Anderson et al. 2014; Alam et al. 2017).

2.3.1 BAO modelling

Our template combines the supercluster infall of linear theory (Kaiser 1987) and the Finger of God (FoG) effect from non-linear growth of structure.

In Fourier space, we use the following template for the two-dimensional non-linear power spectrum

$$P_t(k,\mu) = (1+\beta\mu^2)^2 F(k,\mu,\Sigma_s)P_{\rm dw}(k,\mu). \tag{10}$$

The $(1+\beta\mu^2)^2$ term describes the Kaiser effect (Kaiser 1987) – distortion caused by coherent infall of objects towards the cluster centre. Here, $\beta = f/b$ where f is the cosmological growth rate of structure and b is the large-scale bias. The $F(k,\mu,\Sigma_s)$ factor represents the FoG effect – elongation in the redshift space galaxy distribution along the line-of-sight direction given rise by large random velocities in inner virialized clusters. We model the FoG factor (Park et al. 1994; Peacock & Dodds 1994) as

$$F(k,\mu,\Sigma_s) = \frac{1}{1+k^2\mu^2\Sigma_s^2}, \tag{11}$$

where Σ_s denotes the streaming parameter to account for the dispersion due to random peculiar velocities within clusters. See White et al. (2015) for a comprehensive discussion of various streaming models.

The 'de-wiggled' power spectrum $P_{\rm dw}$ in the template takes the form

$$P_{\rm dw}(k,\mu) = [P_{\rm lin}(k) - P_{\rm nw}(k)]\exp\left[-\frac{k_\parallel^2\Sigma_\parallel^2 + k_\perp^2\Sigma_\perp^2}{2}\right] + P_{\rm nw}(k). \tag{12}$$

In the equation above, $P_{\rm lin}(k)$ is the linear power spectrum (Lewis, Challinor & Lasenby 2000). $P_{\rm nw}(k)$ is the no-wiggle power spectrum (Eisenstein & Hu 1998) that removes the baryonic wiggles. In the de-wiggled power spectrum template, the Gaussian damping term models the degradation of the BAO due to non-linear structure growth. Redshift space distortions make this damping anisotropic, which is captured by different parallel and perpendicular streaming scales $\Sigma_{\parallel}$ and $\Sigma_\perp$ along and across the line of sight. In our analyses, we fix $\Sigma_\perp = 3\,h^{-1}\,\mathrm{Mpc}$ and $\Sigma_\parallel = 6\,h^{-1}\,\mathrm{Mpc}$. These values are based on estimates of the streaming parameters (Crocce & Scoccimarro 2006, 2008; Matsubara 2008) at median redshift of the sample $z = 1.5$. We also vary these parameters and find the fitting result to be insensitive to these choices.

The 2D power spectrum template can be decomposed into multipole moments as

$$P_{\ell,t} = \frac{2\ell+1}{2}\int_{-1}^{1} P_t(k,\mu)L_\ell(\mu)\mathrm{d}\mu, \tag{13}$$

where L_ℓ is the Legendre polynomial. The correlation function multipoles and power spectrum multipoles are Fourier transform pairs and can be obtained as

$$\xi_{\ell,t} = i^\ell \int \frac{k^3 d\log k}{2\pi^2} P_{\ell,t}(k) j_\ell(kr). \tag{14}$$

2.3.2 Modelling the mis-estimate of cosmology

The difference between the true and fiducial cosmology distorts the calculated correlation function. We review how the distorted correlation function can be modelled in terms of the 'isotropic dilation' and 'anisotropic warping' parameters α and ϵ. The approach here is the same as in section 2.2 of Zhu et al. (2016) and we refer the readers to that paper for details. In summary, using α and ϵ, we model the 'true' quasar separation vector and line-of-sight angles, relative to fiducial values, as

$$r = \alpha r^{\rm f}\sqrt{(1+\epsilon)^4(\mu^{\rm f})^2 + (1+\epsilon)^{-2}[1-(\mu^{\rm f})^2]} \tag{15}$$

$$\mu = \cos[\arctan[(1+\epsilon)^{-3}\tan(\arccos\mu^{\rm f})]]. \tag{16}$$

In the above equations, the superscript 'f' denotes quantities measured in the fiducial cosmology.

Given α_0 and α_1, we can calculate $\alpha(z)$ and $\epsilon(z)$ within the redshift range of the sample. These α and ϵ indicate how r and μ

[1] Also see White (2014) and Vlah, Castorina & White (2016) for a more advanced perturbation theory-based template.

are distorted at different redshifts, allowing us to incorporate the mis-estimate of the cosmology into model correlation functions.

3 DATA SETS

3.1 SDSS DR14 quasar sample

The observational data set is the eBOSS (Dawson et al. 2016) quasar sample released as part of the SDSS-IV (Blanton et al. 2017). The survey has an effective area of 1192 deg^2 in the Northern Galactic Cap (NGC) and 857 deg^2 in the Southern Galactic Cap (SGC). The quasar target selection is presented in Ross et al. (2012) and Myers et al. (2015). Quasars that do not have a known redshift are selected for spectroscopic observation. Spectroscopy is obtained through the BOSS double-armed spectrographs (Smee et al. 2013). In our DR14 sample, we applied veto masks as in Reid et al. (2016). To correct for missing targets, redshift failures, fibre collisions, depth dependency, and Galactic extinction, we utilize completion weights and systematic weights according to Laurent et al. (2017) and Ross et al. (2017).

3.2 Simulations

We validate the redshift weighting method by implementing the algorithm on 1000 mock catalogues. These catalogues simulate the clustering of eBOSS DR14 quasars based on the 'quick particle mesh' (QPM) method (White, Tinker & McBride 2014). Each N-body simulation utilizes 2560^3 particles in a box of side length $5120\,h^{-1}$ Mpc. The simulations assume a flat Λ cold dark matter (ΛCDM) cosmology, with $\Omega_m = 0.31$, $\Omega_b h^2 = 0.0220$, $h = 0.676$, $n_s = 0.97$, and $\sigma_8 = 0.8$. Each simulation is initialized by using the second-order Lagrangian perturbation at $z = 25$. The catalogues cover the redshift extent of $0.8 < z < 2.2$ for both the NGC and SGC of the eBOSS footprint. The halo occupation of quasars is parametrized according to the five-parameter halo occupation distribution presented in Tinker et al. (2012).

Rotating the orientations of the 100 simulated cubic boxes, we identify four configurations with less than 1.5 per cent overlap. This enables us to produce 400 QPM mocks for both Galactic caps. Veto masks are applied in the same way as for the data. FKP weights (Feldman et al. 1994) are applied assuming $P_0 = 6000\,h^{-3}$ Mpc^3. Redshift smearing is applied according to Dawson et al. (2016). For specifics of these eBOSS quasar mocks, we refer the readers to Ata et al. (2017).

4 ANALYSIS

4.1 Computing the weighted correlation functions

We analyse the mock catalogues in a similar manner as previous BOSS analyses (Anderson et al. 2014; Alam et al. 2017). In this section, we focus on the steps involving redshift weighting. We also point out that we do not apply density field reconstruction (Eisenstein et al. 2007b), as it is not expected to be efficient or significant for this sample because of the low density of quasars.

To compute the weighted correlation functions from the catalogues, we modify the Landy–Szalay estimator (Landy & Szalay 1993). In addition to weighting each quasar/random by the FKP weight, we weight each quasar/random pairs by x to construct the x-weighted correlation functions. Since a pair that contributes to the BAO signal is close in redshift, we use the pair's mean redshift to calculate x. The weighted 2D correlation functions are given by

$$\xi_w^{\rm data}(r,\mu) = \frac{\widetilde{DD}(r,\mu) - 2\widetilde{DR}(r,\mu) + \widetilde{RR}(r,\mu)}{RR(r,\mu)} \tag{17}$$

where $\widetilde{DD}$, $\widetilde{DR}$, and $\widetilde{RR}$ include the additional pair weight, whereas RR in the denominator does not. We decompose the 2D correlation functions and calculate the monopoles and quadrupoles as

$$\xi_{\ell,w}^{\rm data}(r) = \frac{2\ell+1}{2}\int_{-1}^{1}\xi_w^{\rm data}(r,\mu)L_\ell(\mu){\rm d}\mu. \tag{18}$$

We consider two cases: an unweighted sample using only the FKP weight and a weighted sample uses both the '1' and 'x' weights. For both cases, we treat the quasar sample as a unified one without splitting it into redshift bins.

4.1.1 *The fitting model*

We define our fitting model

$$\xi_{\ell,w}^{\rm fit}(r) = B_w^2\xi_{\ell,w}(r) + A_{\ell,w}(r), \tag{19}$$

where $\xi_{\ell,w}(r)$ is the weighted correlation function and $A(r)$ is a nuisance polynomial to marginalize out un-modelled broad-band features. These signals include redshift space distortions and scale-dependent bias. We assume

$$A_{\ell,w}(r) = \frac{a_{\ell,w,1}}{r} + a_{\ell,w,2}. \tag{20}$$

We allow a multiplicative factor $B_w^2 \sim 1$ to float to determine the overall amplitudes of the monopole and quadrupole, while β adjusts the relative amplitude between the two.

In our fiducial weighted fits, we use a total of 13 fitting parameters: α_0, α_1, β, B_1, B_x, and 8 nuisance parameters to absorb the broad-band features. We use the fiducial fitting range $48 < r < 184h^{-1}$ Mpc with 8 h^{-1} Mpc bins.

4.2 Parameter inference

We assume the likelihood function is a multivariate Gaussian. The posterior distribution of α_0 and α_1 can be written as

$$p(\alpha_0,\alpha_1) \propto e^{-\chi^2(\alpha_0,\alpha_1)/2} \tag{21}$$

where χ^2 is given by

$$\chi^2 = \mathbf{D}\mathbf{C}^{-1}\mathbf{D}^T, \tag{22}$$

where $\mathbf{C}$ represents the covariance matrix and $\mathbf{D}$ is the vector difference between the data and model. We calculate $\mathbf{C}$ as the sample covariance matrix from the mocks and apply the correction factor (Hartlap, Simon & Schneider 2007; Percival et al. 2014) to account for the skewness of the inverse Wishart distribution.

Given α_0 and α_1, we minimize the χ^2 via a downhill simplex algorithm (Nelder & Mead 1965) designed to handle the non-linear parameters. We fit the linear nuisance parameters by a nested least-squares. The simplex algorithm searches for the best-fitting parameters by finding the minimum χ^2 within the non-linear parameter space.

We calculate the likelihood surface through computing best-fitting χ^2 on a two-dimensional grid for $0.7 < \alpha_0 < 1.3$ and $-0.5 < \alpha_1 < 0.5$ at spacings of 0.01 and 0.02, respectively. The likelihood surface enables one to calculate the distribution of α_0 and α_1. The low signal-to-noise BAO feature of some mocks causes the nuisance polynomial to dominate the model correlation function.

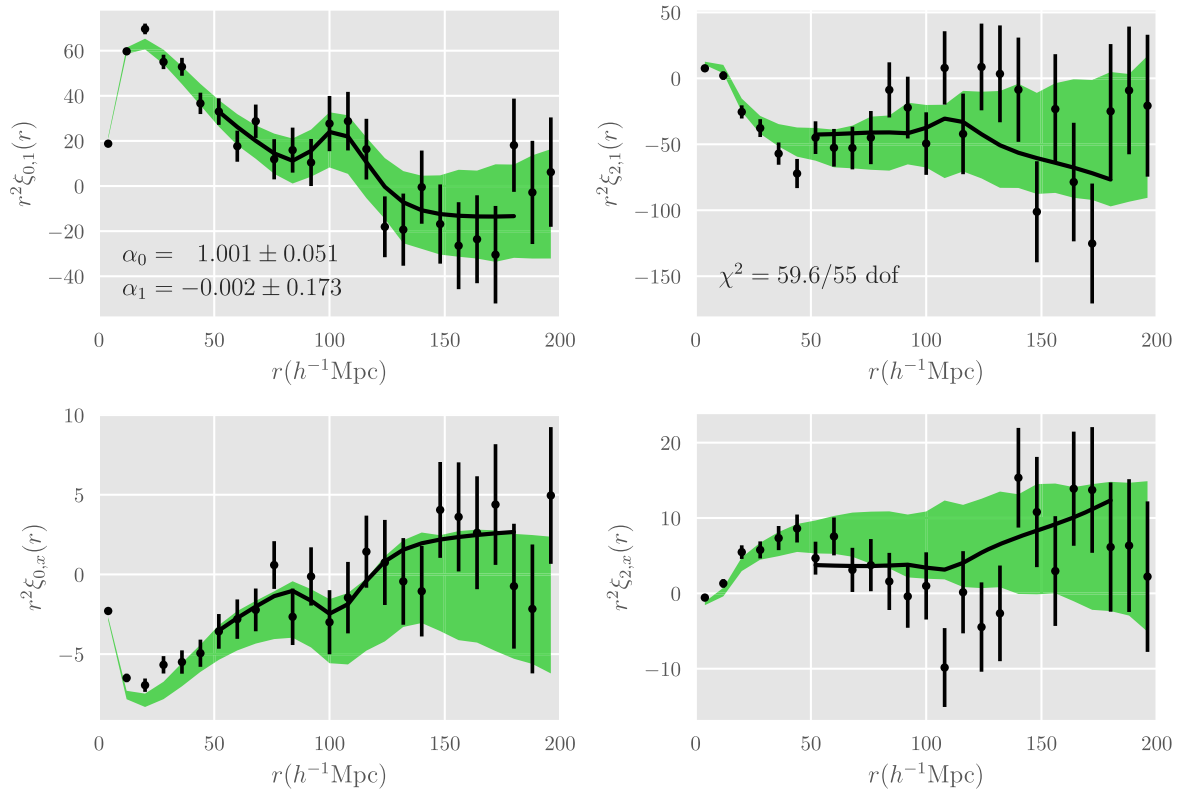

Figure 1. The DR14 quasar correlation function and the average QPM mock correlation functions. The black circles with error bars are the correlation function multipoles from the DR14 sample. The top panels display the 'unweighted' monopoles (left) and quadrupoles (right); the bottom pair displays the 'x-weighted' ones. The associated error bars are 1σ errors of the mocks. The solid black line passing through the black points show the best fitting to the DR14 points with relevant statistics on the top panels. The green bands in each on the figure represent the average monopoles (left) and quadrupoles (right) from the 400 mocks with 1 standard deviation errors. The bands plotted are errors of an individual mock, which are $\sqrt{400}$ times larger than that of the average correlation function. The 'x-weighted' monopoles and quadrupoles show an inverted shape because of an overall negative weight.

To address this issue, we place a Gaussian prior on β centred at 0.4 with width 0.2. We also adopt a Gaussian prior on B_1^2 and B_x^2 at 1 with width 0.2. To suppress the unphysical downturns in χ^2, we have applied Gaussian priors of width 0.1 centred around $\alpha_0 = 1$ and width 0.2 centred around $\alpha_1 = 0$. These priors do not dominate our calculation of the likelihood of α_0 and α_1. Their implications are discussed in more detail in Section 5.

5 RESULTS

The fits to the mock correlation functions assume the QPM cosmology as the fiducial cosmology using a pivot redshift $z_0 = 1.8$. The fitting model and procedure are sketched out in Section 4.

Fig. 1 shows the DR14 quasar correlation functions and the average of these from 400 mocks. The DR14 quasar correlation functions are indicated as points with error bars. The bands in the figure correspond to the 1σ error for individual mocks. The mocks are consistent with the DR14 points. The quadrupole moments show significant noise. Despite the uncertainties, the monopole moments demonstrate a clearly visible acoustic feature in both the '1-weighted' and 'x-weighted monopoles.

The thick black line is the best fitting to the DR14 data points with relevant statistics labelled on the figure. In the fiducial case, we measure $\alpha_0 = 1.001 \pm 0.051$ and $\alpha_1 = -0.002 \pm 0.173$. The 'unweighted' fits without redshift weighting yield $\alpha_0 = 1.003 \pm 0.041$ and $\alpha_1 = -0.004 \pm 0.136$. The distribution of α_0 and α_1 measured from the DR14 quasar sample is shown in Fig. 2. For the DR14 sample, applying redshift weighting does not yield reduction in the size of the error bars for the measured α_0 and α_1.

We test the robustness of our result by varying various aspects of the fit including the fitting range, binning, streaming parameters, and pivot redshift. The results all agree within 1σ uncertainties. Table 1 presents a summary of our fitting results. In the table, *poly*3 corresponds to fitting with a third degree nuisance polynomial of the form $A(r) = a_1/r^2 + a_2/r + a_3$. In addition, we perform an isotropic BAO fit by setting $\alpha_1 = 0$ and only allowing α_0 to vary. This analysis produces $\alpha_0 = 0.996 \pm 0.031$, consistent with the result 0.994 ± 0.037 in Ata et al. (2017). The small discrepancy in the error could be due to differences in the applied priors, as Ata et al. (2017) restricts to the prior range $0.8 < \alpha < 1.2$. In our calculation of the likelihood, we use a larger prior range $0.7 < \alpha_0 < 1.3$ and a Gaussian prior of width 0.1 centred around $\alpha_0 = 1$.

To validate our methodology, we fit 400 QPM mocks and measure α_0 and α_1. Since we use the simulation cosmology as our fiducial cosmology, we anticipate our measurements to agree with $\langle\alpha_0\rangle = 1$ and $\langle\alpha_1\rangle = 0$ within uncertainty if the measurements are unbiased. A summary of the mock results can be found in Table 1. We indeed verify our method to yield unbiased estimators of α_0 and α_1.

The errors of α_0 and α_1 measured from the 400 QPM mocks are indicated as blue points in Fig. 3. The orange points in the background show the errors from the 'unweighted' fits. The fitted

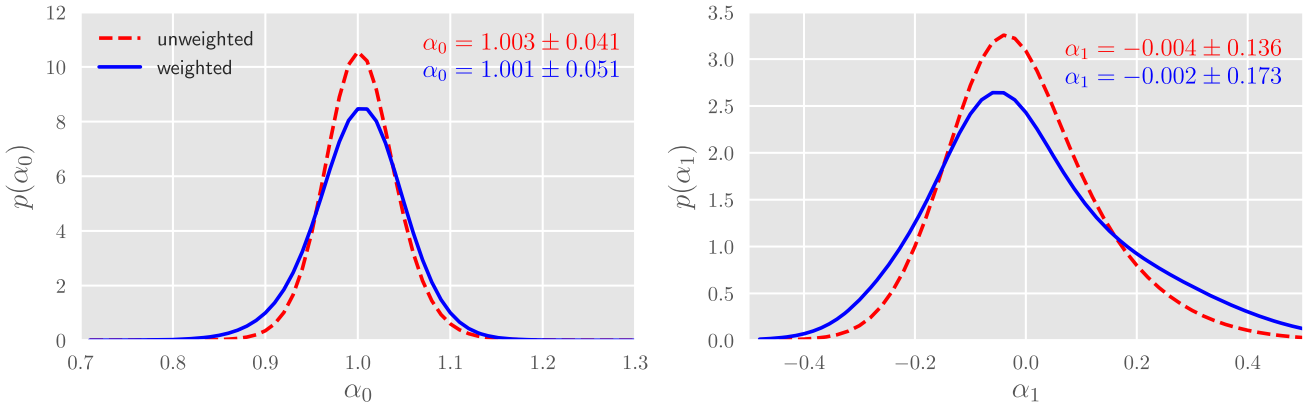

Figure 2. Distribution of α_0 and α_1 from the DR14 fits. The left- and right-hand panels show the derived $p(\alpha_0)$ and $p(\alpha_1)$ distributions, respectively. The red dashed lines represent the distribution from fitting the 'unweighted' estimator; the blue solid lines correspond to the sharpened distribution we obtained from applying redshift weighting. The mean and standard deviation of both distributions are labelled in the panels.

Table 1. BAO fitting results of the DR14 quasar data and QPM mocks. Our fiducial analysis assumes a pivot redshift of $z_0 = 1.8$ and a fitting range of $48 < r < 184h^{-1}$ Mpc with $8h^{-1}$ Mpc binning. The fiducial analysis utilizes redshift weighting. The mock results shown here are the inverse variance weighted average of the 400 QPM mock fits.

Model	α_0	α_1
	DR14 results	
Fiducial	1.001 ± 0.051	0.002 ± 0.173
Fiducial, unweighted	1.003 ± 0.041	-0.004 ± 0.136
Fit w/ $\Sigma_s = 2\ h^{-1}$ Mpc	1.004 ± 0.052	0.014 ± 0.172
$(\Sigma_\perp, \Sigma_\parallel) = (4, 8)\ h^{-1}$ Mpc	1.002 ± 0.051	0.007 ± 0.172
Fi w/ poly3	1.001 ± 0.048	-0.023 ± 0.175
Fit w/o x-weighted quadrupole	1.006 ± 0.043	0.013 ± 0.134
α_0 only	0.996 ± 0.031	–
$48 < r < 136\ h^{-1}$ Mpc	0.999 ± 0.053	-0.015 ± 0.167
$48 < r < 160\ h^{-1}$ Mpc	0.987 ± 0.061	-0.009 ± 0.193
$\Delta r = 4\ h^{-1}$ Mpc	0.997 ± 0.049	0.090 ± 0.165
$z_{\rm pivot} = 1.2$	1.002 ± 0.072	-0.002 ± 0.131
$z_{\rm pivot} = 2$	0.999 ± 0.049	0.001 ± 0.179
	Mock results	
Fiducial	0.992 ± 0.052	0.001 ± 0.141
Fiducial, unweighted	0.998 ± 0.054	0.014 ± 0.157
Fit w/ $\Sigma_s = 2\ h^{-1}$ Mpc	0.993 ± 0.054	0.003 ± 0.144
$(\Sigma_\perp, \Sigma_\parallel) = (4, 8)\ h^{-1}$ Mpc	0.992 ± 0.052	0.003 ± 0.141
Fit w/ poly3	0.991 ± 0.053	0.001 ± 0.147
Fit w/o x-weighted quadrupole	0.993 ± 0.052	0.001 ± 0.143
$48 < r < 136\ h^{-1}$ Mpc	0.988 ± 0.055	-0.006 ± 0.143
$z_{\rm pivot} = 1.2$	0.991 ± 0.067	-0.014 ± 0.115
$z_{\rm pivot} = 2$	0.993 ± 0.050	-0.001 ± 0.146
	'4x' Mock results	
'4x' mocks, fiducial	0.995 ± 0.028	0.001 ± 0.077
'4x' mocks, unweighted	0.996 ± 0.031	0.017 ± 0.105
'4x' mocks, $z_{\rm pivot} = 1.2$	0.993 ± 0.040	-0.001 ± 0.060
'4x' mocks, $z_{\rm pivot} = 2$	0.996 ± 0.026	-0.001 ± 0.081

DR14 data point is also displayed. The mock α_0 and α_1 errors are representative of the DR14 errors.

We compare the σ_{α_0} and σ_{α_1} obtained from the 'unweighted' and 'weighted' analysis mock by mock. Among the 400 mock measurements, 221 produce an improved σ_{α_0}, and 275 show an improved σ_{α_1} when we apply the redshift weights. These values

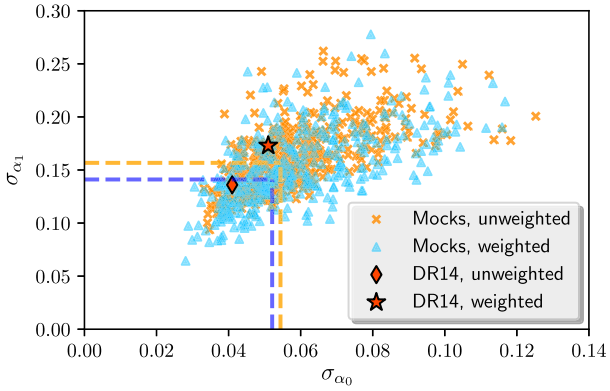

Figure 3. The σ_{α_0} and σ_{α_1} values measured from the 400 mocks and from the DR14 sample. The blue triangles correspond to the 'weighted' measurement errors and the orange triangles are the 'unweighted' values. The errors denoted by the horizontal and vertical dashed lines are the errors of the inverse variance weighted average of the mock results, multiplied by $\sqrt{400}$ for ease of comparison with individual mock points. Our DR14 σ_{α_0} and σ_{α_1} are labelled as the red star ('weighted') and diamond ('unweighted'). The DR14 point situates within the locus of mock points.

correspond to 55 per cent and 69 per cent of the mocks. Given the magnitude of these percentages, it is not surprising that redshift weighting does not yield smaller σ_{α_0} and σ_{α_1} errors for the current DR14 sample.

Overall, however, redshift weighting does shrink the measured error bars. We aggregate the mock measurements of α_0 and α_1 through inverse variance weighting to minimize the variance of the weighted average. Each mock measurement of α_0 and α_1 is weighted in inverse proportion to its variance. We obtain this weighted average as $\hat{\alpha} = \frac{\sum \alpha_i/\sigma^2_{\alpha_i}}{\sum 1/\sigma^2_{\alpha_i}}$. The summation is performed over the 400 mocks. The error of $\hat{\alpha}$ is given by $\sigma(\hat{\alpha}) = 1/\sqrt{\sum \frac{1}{\sigma^2_{\alpha_i}}}$. This error is scaled by $\sqrt{400}$ for ease of comparison with errors from individual mock measurements. The aggregated mock statistics are presented in Table 1. We observe a decrease in σ_{α_1} from 0.157 without redshift weights to 0.141 with redshift weights. This change corresponds to a 10 per cent decrease. We will further comment on the magnitude of this improvement in Section 6.

Table 2. Constraints on $D_M(r_{\rm d,\,fid}/r_{\rm d})$ and $H(r_{\rm d}/r_{\rm d,\,fid})$ measured from the DR14 quasar sample from our analysis with redshift weighting. Also listed are the derived spherically averaged distance measurements $D_V(r_{\rm d,\,fid}/r_{\rm d})$ from our D_M and H measurements. The measurements at different redshifts are correlated.

Redshift	$D_M(r_{\rm d,\,fid}/r_{\rm d})$ (Mpc)	$H(r_{\rm d}/r_{\rm d,\,fid})$ (km s^{-1} Mpc^{-1})	$D_V(r_{\rm d,\,fid}/r_{\rm d})*$ (Mpc)
0.8	2876 ± 304	106.9 ± 4.9	2646 ± 205
1.0	3405 ± 305	120.7 ± 7.3	3065 ± 182
1.5	4491 ± 272	161.4 ± 30.9	3840 ± 182
2.0	5325 ± 249	189.9 ± 32.9	4356 ± 300
2.2	5606 ± 255	232.5 ± 54.6	4514 ± 359

The joint likelihood distribution of α_0 and α_1 allows us an estimate to be made of the joint distribution of χ and H. To perform this calculation, we first draw random variables from the joint distribution of α_0 and α_1. We reconstruct the distance–redshift relation $\chi(z)$ and Hubble parameter $H(z)$ from equations (1) and (2) with the drawn α_0 and α_1. This approach enables us to obtain an estimated joint distribution of χ and H. It is then straightforward to calculate statistics of χ and H. Since these χ and H measurements at different redshifts are derived from the same model of the distance–redshift relation, they are highly correlated. To use our result for cosmological comparisons, it is advisable to directly use the joint likelihood distribution of α_0 and α_1 we measured.

Our parametrization of the distance–redshift relation and Hubble parameter allows one to obtain constraints for both across the redshift range of the sample. In Table 2, we produce $D_{\rm M}$ and H measurements at several redshifts. We also derive spherically averaged distance measurement D_V from our D_M and H measurements. The measurements at these redshifts are highly correlated. We thus report the correlation matrix for D_M and H at only two redshifts $z_1 = 1$ and $z_2 = 2$ below as

$$\mathbf{C} = \begin{array}{c} \begin{matrix} D_M(z_1) & H(z_1) & D_M(z_2) & H(z_2) \end{matrix} \\ \begin{pmatrix} 1 & 0.25 & 0.72 & 0.66 \\ & 1 & -0.48 & 0.85 \\ & & 1 & 0.00 \\ & & & 1 \end{pmatrix} \end{array} \begin{matrix} D_M(z_1) \\ H(z_1) \\ D_M(z_2) \\ H(z_2). \end{matrix} \tag{23}$$

The correlation between $D_M(z = 1)$ and $D_M(z = 2)$ is quite substantial, as is the correlation between H at $z = 1$ and $z = 2$. However, at both redshifts, the correlation between D_M and H is low. This behaviour is not necessarily the case for a different choice of z_1 and z_2. There is a tradeoff between the correlation of D_M and H at the same redshift and the correlation between z_1 and z_2.

In analyzing the BAO from the BOSS DR 12 galaxy mock catalogues, Zhu et al. (2016) reported that the distance and Hubble parameter measurements are insensitive to the choice of pivot redshifts. Our mock measurements confirm this finding.

At different pivot redshifts, a large error in α_0 is usually compensated by a smaller error in α_1, and vice versa. Table 1 lists fitting results at three different pivot redshifts $z_0 = 1.2$, 1.8, and 2. Selecting $z_0 = 2$ yields the smallest σ_{α_0} but has the largest σ_{α_1}. Conversely, $z_0 = 1.2$ yields the largest σ_{α_0} but has the smallest σ_{α_1}. When reconstructing D_M and H constraints from α_0 and α_1, the error from the two parameters compensate one another and makes the distance and Hubble parameter constraints insensitive to the choice of the pivot redshift.

We compare our results with recent measurements of D_M and H. Fig. 4 displays our D_M and H measurements along with the ΛCDM prediction from Planck (Planck Collaboration 2016). Our distance and Hubble parameter measurements are in agreement with the Planck results within the 1σ uncertainty. We also show similar measurements in the literature: the BOSS DR12 results from Alam et al. (2017), the BOSS Ly α from Bautista et al. (2017), and the cross correlation of Ly α forest and quasars from Font-Ribera et al. (2014). These measurements provide both distance and Hubble parameter measurements at the effective redshift of their respective samples. Additional spherically averaged distance measurements (D_V) are 6dFGS Beutler et al. (2011), SDSS MGS Ross et al. (2015), WiggleZ Kazin et al. (2014), and eBOSS DR14 isotropic BAO Ata et al. (2017). In particular, the DR14 isotropic BAO result (labelled as 'DR14-Iso' in Fig. 4) analyses the same sample as our work and reports a spherically averaged distance measurement of $D_V(z = 1.52) = 3843 \pm 147\,(r_{\rm d,fid}/r_{\rm d})$ Mpc. As a comparison, we derive spherically averaged distance measurement from our D_M and H measurements at the same redshift and obtain $D_V(z = 1.52) = 3871 \pm 157\,(r_{\rm d}/r_{\rm d,fid})$ Mpc without redshift weighting and $3860 \pm 204\,(r_{\rm d,\,fid}/r_{\rm d})$ Mpc with redshift weighting. These measurements are all consistent with Ata et al. (2017) measurement. In addition, we note that our Hubble parameter measurement spans a redshift range ($0.8 < z < 2.2$) that has not been measured in previous redshift surveys.

6 FINAL SAMPLE OUTLOOK

The DR14 quasar sample covers 1192 deg^2 and 852 deg^2 of NGC and SGC regions. This solid angle is approximately a quarter of the final footprint of 7500 deg^2 for clustering quasars. The quadruple increase in footprint will result in reduced noise in the final sample. In this section, we assess the outlook of BAO measurements as would be obtained from the final eBOSS sample.

To mimic the noise level in the final sample clustering quasars, we average the correlation functions from every four mock catalogues. This simple averaging serves to reflect the quadruple increase in footprint. After the averaging, we obtain 100 averaged mock correlation functions (labelled '4x' mocks) from the original 400 QPM mocks. We indeed observe greatly reduced noise in these '4x' mock correlation functions.

We analyse the aforementioned 100 '4x' mock correlation functions with the same method described in Section 4. The fitting results of these mocks are unbiased (see Table 1). Fig. 5 presents the errors σ_{α_0} and σ_{α_1} measured from the 100 '4x' mocks. We aggregate the mock measurements of α_0 and α_1 by calculating the inverse variance weighted average by $\hat{\alpha} = \frac{\sum \alpha_i/\sigma^2_{\alpha_i}}{\sum 1/\sigma^2_{\alpha_i}}$. The summation is over the 100 '4x' mocks. The error of $\hat{\alpha}$ is given by $\sigma(\hat{\alpha}) = 1/\sqrt{\sum \frac{1}{\sigma^2_{\alpha_i}}}$. We scale this error by $\sqrt{100}$ for ease of comparison with individual '4x' mock errors. The vertical and horizontal dashed lines in Fig. 5 show these statistics. The error $\sigma_{\hat{\alpha}_0}$ decreases from 3.1 per cent to 2.8 per cent. Similarly, the weighted analysis gives an error of $\sigma_{\hat{\alpha}_1}$ of 7.7 per cent, compared to a 10.5 per cent without redshift weighting. These results correspond to a 10 per cent improvement in α_0 and a 27 per cent improvement in α_1.

Among the 100 '4x' mock measurements, 83 have an improved σ_{α_0} and 89 show an improved σ_{α_1} when we apply the redshift weights. This behaviour can be clearly seen in Fig. 6. The dashed line in the figure corresponds to a straight line of unit slope. The majority of points fall below this equality line. Redshift weighting produces improved measurement errors for more than 80 per cent of the '4x' mocks, demonstrating that although redshift weighting

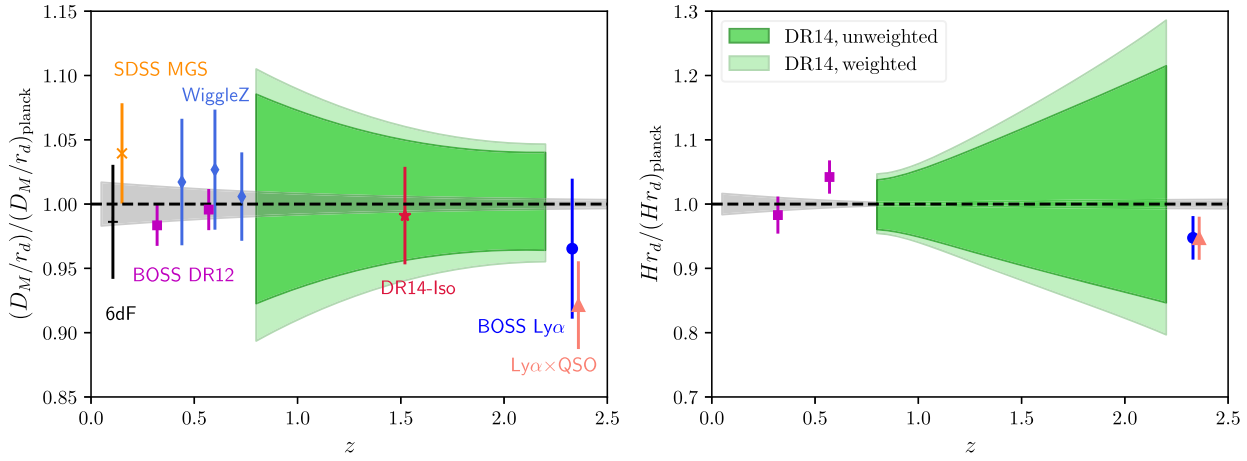

Figure 4. Our DR14 D_M and H measurements from 'unweighted' and 'weighted' analyses compared to the Planck flat-ΛCDM predictions. All error bands and error bars correspond to 1 standard deviation errors. Our DR14 measurements (green bands) are consistent with the Planck results (grey bands) within uncertainty. We emphasize that the D_M and H measurements at different redshifts are highly correlated. We also show several recent measurements for comparison, some of which are spherically averaged BAO distance measurements (D_V). See texts for descriptions of these additional measurements.

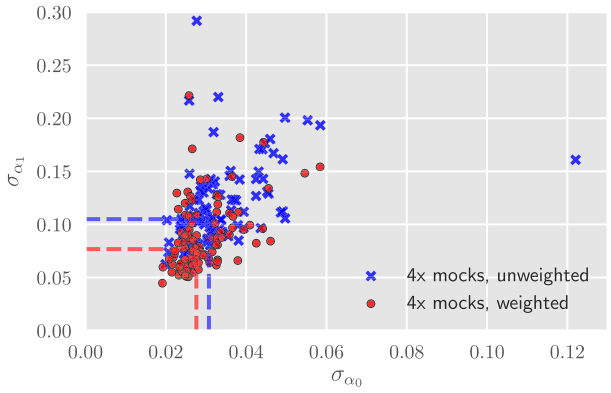

Figure 5. The σ_{α_0} and σ_{α_1} values measured from the '4x' mocks. The measurements without redshift weighting are denoted by blue crosses, while the ones with redshift weighting are denoted by red circles. The vertical and horizontal dashed lines correspond to the error of inverse variance weighted mean of α_0 and α_1 from the mocks, multiplied by $\sqrt{100}$ for easy comparison with individual '4x' mock points.

does not yield smaller σ_{α_0} and σ_{α_1} for the current sample, it will likely be efficient for the final quasar sample.

The gains from redshift weighting in the '4x' mocks are much more significant than in the original QPM mocks. This result occurs because some mocks among the 400 individual QPM mocks are quite noisy and possess a weak BAO feature. As a result, these weak BAO detections lead to non-Gaussian likelihood surface. While redshift weighting is powerful at turning a 'mediocre' measurement into a 'good' one, it cannot turn a 'bad' measurement (a non-detection of the BAO feature, for example) into a 'mediocre' or 'good' measurement. These noisy mocks thus render redshift weighting not as effective. After averaging, the '4x' mocks have better signal-to-noise ratio and enhanced BAO features. In fitting the '4x' mocks, the number of weak and non-detections is significantly reduced an redshift weighting thus becomes much more efficient in tightening the error bars. The substantial gains demonstrated in the '4x' mocks suggest redshift weighting will play an important role in unlocking the full potential of the BAO constraints from the final quasar sample.

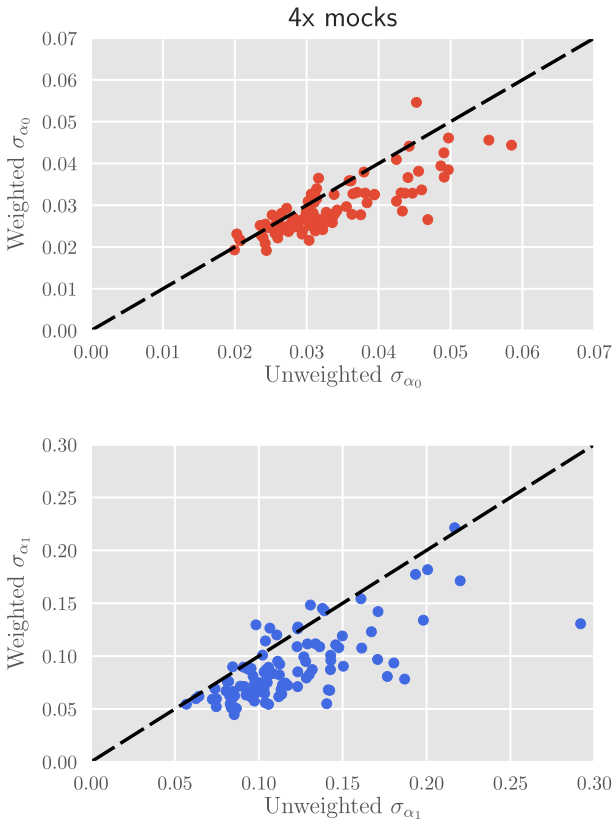

Figure 6. The weighted and unweighted σ_{α_0} and σ_{α_1} values measured from the 100 '4x' mocks. The dashed line in the figure corresponds to a straight line of unit slope. The majority of points lie below the dashed line, suggesting redshift weighting is likely to be efficient for the final quasar sample.

7 DISCUSSION

The DR14 quasar sample covers a wide redshift range from $z = 0.8$ to 2.2. To analyse the BAO information in such a large range without sacrificing signal-to-noise ratio by splitting the sample into redshift slices, redshift weighting (Zhu et al. 2016) is a natural choice. We

have presented in this paper an anisotropic BAO analysis of the BOSS DR14 quasar sample using this technique.

We first model the distance–redshift relation as a Taylor expansion. Estimating the coefficients of this expansion allows us to reconstruct $D_M(z)$ and $H(z)$ within the range of redshifts of the sample.

We establish the effectiveness of redshift weighting in producing unbiased optimized constraints from a set of mock catalogues. With the same methodology, we analyse the BOSS DR14 quasar sample and achieve improved D_M and H constraints in fitting the BAO feature in the sample. Our D_M error ranges from 4.6 per cent at $z = 2.2$ to 10.5 per cent at $z = 0.8$. Our H error ranges from 4.6 per cent at $z = 0.8$ to 23.5 per cent at $z = 2.2$.

To examine what will be possible when the final quasar sample becomes available, we generate a new set of mock catalogues with smaller noises by averaging every four of the original DR14 mocks to approximate the final eBOSS quasar sample. We analyse these averaged mocks with the same methodology and observe that redshift weighting offers significant improvement in the measurement errors over the single-bin analysis without redshift weighting. This demonstration suggests redshift weighting is important to unlocking the full BAO information within the sample.

The power of redshift weighting lies in its optimal use of the information without splitting the sample into redshift slices. Although one can retain sensitivity to redshift by repeating traditional analyses on multiple slices and properly accounting for covariance between slices, redshift weighting provides a more efficient and straightforward implementation.

The method is especially useful when the survey covers a wide range of redshifts. Its success on the set of mock catalogues that mimic the final quasar sample shows promise that the method will be extremely useful for upcoming surveys like the Dark Energy Spectroscopic Instrument (DESI; DESI Collaboration 2016a,b). An anisotropic BAO analysis with similar redshift weighting techniques in Fourier space will appear in Wang et al. (in preparation). They optimize the measurements by deploying redshift weights constructed for the BAO signal in the quasar power spectrum. Different from how this work utilizes the redshift weights, Wang et al. (in preparation) assign the weights to individual quasars instead of weighting quasar pairs. Apart from this difference, the methodology is similar to Zhu et al. (2016) and this work. Different from the result of this work, Wang et al. (in preparation) find applying redshift weighting on the DR14 sample produces improved measurement over the traditional single-bin analysis. This difference may be due to the difference in methodology and noise properties of the power spectrum and the correlation function. Despite this difference, the results reported in both works are fully consistent with each other within uncertainty. Besides these works, similar analysis methods inspired by the BAO redshift weights have been proposed to constrain redshift space distortions (Ruggeri et al. 2016) and primordial non-Gaussianity (Mueller, Percival & Ruggeri 2017) in upcoming surveys. Redshift Space Distortions measurements on the DR14 sample utilizing a similar methodology will appear in Ruggeri et al. (2018) and Zhao et al. (in preparation). Redshift weighting can bring us closer to realizing the full capabilities of these surveys as we aim towards an ever increasing understanding of the expansion history of the universe.

ACKNOWLEDGEMENTS

FZ would like to thank Tomomi Sunayama for useful conversations. This work was supported in part by the National Science Foundation under grant no. PHYS-1066293. NP and FZ are supported in part by a DOE Early Career grant DE-SC0008080. FB is a Royal Society University Research Fellow.

Funding for the Sloan Digital Sky Survey IV has been provided by the Alfred P. Sloan Foundation, the U.S. Department of Energy Office of Science, and the Participating Institutions. SDSS-IV acknowledges support and resources from the Center for High-Performance Computing at the University of Utah. The SDSS web site is www.sdss.org.

SDSS-IV is managed by the Astrophysical Research Consortium for the Participating Institutions of the SDSS Collaboration including the Brazilian Participation Group, the Carnegie Institution for Science, Carnegie Mellon University, the Chilean Participation Group, the French Participation Group, Harvard-Smithsonian Center for Astrophysics, Instituto de Astrofsica de Canarias, The Johns Hopkins University, Kavli Institute for the Physics and Mathematics of the Universe (IPMU)/University of Tokyo, Lawrence Berkeley National Laboratory, Leibniz Institut fr Astrophysik Potsdam (AIP), Max-Planck-Institut fr Astronomie (MPIA Heidelberg), Max-Planck-Institut fr Astrophysik (MPA Garching), Max-Planck-Institut fr Extraterrestrische Physik (MPE), National Astronomical Observatory of China, New Mexico State University, New York University, University of Notre Dame, Observatrio Nacional/ MCTI, The Ohio State University, Pennsylvania State University, Shanghai Astronomical Observatory, United Kingdom Participation Group, Universidad Nacional Autnoma de Mxico, University of Arizona, University of Colorado Boulder, University of Oxford, University of Portsmouth, University of Utah, University of Virginia, University of Washington, University of Wisconsin, Vanderbilt University, and Yale University.

This research used resources of the National Energy Research Scientific Computing Center, a DOE Office of Science User Facility supported by the Office of Science of the U.S. Department of Energy under Contract No. DE-AC02-05CH11231.

REFERENCES

Abolfathi B. et al., 2018, ApJS, 235, 42
Alam S. et al., 2015, ApJS, 219, 12
Alam S. et al., 2017, MNRAS, 470, 2617
Anderson L. et al., 2014, MNRAS, 441, 24
Ata M. et al., 2018, MNRAS , 473, 4773
Bautista J. E. et al., 2017, A&A, 603, A12
Beutler F. et al., 2011, MNRAS, 416, 3017
Blake C., Collister A., Bridle S., Lahav O., 2007, MNRAS, 374, 1527
Blanton M. R. et al., 2017, AJ, 154, 28
Bond J. R., Efstathiou G., 1987, MNRAS, 226, 655
Cole S. et al., 2005, MNRAS, 362, 505
Crocce M., Scoccimarro R., 2006, Phys. Rev. D, 73, 063519
Crocce M., Scoccimarro R., 2008, Phys. Rev. D, 77, 023533
Dawson K. S. et al., 2013, AJ, 145, 10
Dawson K. S. et al., 2016, AJ, 151, 44
Delubac T. et al., 2015, A&A, 574, A59
DESI Collaboration, 2016a, preprint (arXiv:1611.00036)
DESI Collaboration, 2016b, preprint (arXiv:1611.00037)
Eisenstein D. J., Hu W., 1998, ApJ, 496, 605
Eisenstein D. J. et al., 2005, ApJ, 633, 560
Eisenstein D. J., Seo H.-J., White M., 2007a, ApJ, 664, 660
Eisenstein D. J., Seo H.-J., Sirko E., Spergel D. N., 2007b, ApJ, 664, 675
Eisenstein D. J. et al., 2011, AJ, 142, 72
Feldman H. A., Kaiser N., Peacock J. A., 1994, ApJ, 426, 23
Font-Ribera A. et al., 2014, J. Cosmol. Astropart. Phys., 5, 027
Gunn J. E. et al., 2006, AJ, 131, 2332
Hartlap J., Simon P., Schneider P., 2007, A&A, 464, 399

Hu W., Sugiyama N., 1996, ApJ, 471, 542
Kaiser N., 1987, MNRAS, 227, 1
Kazin E. A. et al., 2010, ApJ, 710, 1444
Kazin E. A. et al., 2014, MNRAS, 441, 3524
Kitaura F.-S. et al., 2016, Phys. Rev. Lett., 116, 171301
Landy S. D., Szalay A. S., 1993, ApJ, 412, 64
Laurent P. et al., 2017, J. Cosmol. Astropart. Phys., 7, 017
Lewis A., Challinor A., Lasenby A., 2000, ApJ, 538, 473
Matsubara T., 2008, Phys. Rev. D, 77, 063530
Mueller E.-M., Percival W. J., Ruggeri R., 2017, preprint (arXiv:1702.05088)
Myers A. D. et al., 2015, ApJS, 221, 27
Nelder J. A., Mead R., 1965, Comput. J., 7, 308
Padmanabhan N., White M., 2008, Phys. Rev. D, 77, 123540
Padmanabhan N., Xu X., Eisenstein D. J., Scalzo R., Cuesta A. J., Mehta K. T., Kazin E., 2012, MNRAS, 427, 2132
Park C., Vogeley M. S., Geller M. J., Huchra J. P., 1994, ApJ, 431, 569
Peacock J. A., Dodds S. J., 1994, MNRAS, 267, 1020
Peebles P. J. E., Yu J. T., 1970, ApJ, 162, 815
Percival W. J. et al., 2010, MNRAS, 401, 2148
Percival W. J. et al., 2014, MNRAS, 439, 2531
Planck Collaboration, 2016, A&A, 594, A13
Reid B. et al., 2016, MNRAS, 455, 1553
Ross N. P. et al., 2012, ApJS, 199, 3
Ross A. J., Samushia L., Howlett C., Percival W. J., Burden A., Manera M., 2015, MNRAS, 449, 835
Ross A. J. et al., 2017, MNRAS, 464, 1168
Ruggeri R., Percival W., Gil-Marín H., Zhu F., Zhao G., Wang Y., 2016, MNRAS, 464, 2698
Ruggeri R. et al., 2018, preprint (arXiv:1611.00036)
Smee S. A. et al., 2013, AJ, 146, 32
Sunyaev R. A., Zeldovich Y. B., 1970, Ap&SS, 7, 3
Tegmark M., Taylor A. N., Heavens A. F., 1997, ApJ, 480, 22
Tinker J. L. et al., 2012, ApJ, 745, 16
Vlah Z., Castorina E., White M., 2016, J. Cosmol. Astropart. Phys., 12, 007
White M., 2014, MNRAS, 439, 3630
White M., Tinker J. L., McBride C. K., 2014, MNRAS, 437, 2594
White M., Reid B., Chuang C.-H., Tinker J. L., McBride C. K., Prada F., Samushia L., 2015, MNRAS, 447, 234
Xu X., Cuesta A. J., Padmanabhan N., Eisenstein D. J., McBride C. K., 2013, MNRAS, 431, 2834
Zhao G.-B. et al., 2016, MNRAS, 457, 2377
Zhu F., Padmanabhan N., White M., 2015, MNRAS, 451, 236
Zhu F., Padmanabhan N., White M., Ross A. J., Zhao G., 2016, MNRAS, 461, 2867

[1]*Department of Physics, Yale University, New Haven, CT 06511, USA*
[2]*Center for Cosmology and Astroparticle Physics, Department of Physics, The Ohio State University, OH 43210, USA*
[3]*Department of Physics and Astronomy, U.C. Berkeley, Berkeley, CA 94720, USA*
[4]*Institute of Cosmology, Gravitation, University of Portsmouth, Dennis Sciama Building, Portsmouth, PO1 3FX, UK*
[5]*National Astronomy Observatories, Chinese Academy of Science, Beijing 100012, P.R. China*
[6]*Lawrence Berkeley National Lab, 1 Cyclotron Rd, Berkeley CA 94720, USA*
[7]*IRFU, CFA, Université Paris-Scalay, F-91191 Gif-sur-Yvette, France*
[8]*Sorbonne Universités, Institut Lagrange de Paris (ILP), 98 bis Boulevard Arago, 75014 Paris, France*
[9]*Laboratoire de Physique Nucléaire et de Hautes Energies, Université Pierre et Marie Curie, 4 Place Jussieu, 75005 Paris, France*
[10]*Department of Physics and Astronomy, University of Utah, 115 S. 1400 E., Salt Lake City, UT 84112, USA*
[11]*Apache Point Observatory, PO Box 59, Sunspot, NM 88349, USA*
[12]*Instituto de Física, Universidad Nacional Autónoma de México, Apdo.Postal 20-364, 01000 México D.F., México*
[13]*Department of Physics and Astronomy, Sejong University, Seoul 143-747, Korea*
[14]*Department of Astronomy and Astrophysics, The Pennsylvania State University, University Park, PA 16802, USA*
[15]*Institute for Gravitation and the Cosmos, The Pennsylvania State University, University Park, PA 16802, USA*
[16]*School of Physics and Astronomy, University of St Andrews, North Haugh, St Andrews KY16 9SS, UK*

This paper has been typeset from a TEX/LATEX file prepared by the author.